Ambient Hydrocarbon Detection with an

Ultralow-loss Cavity Raman Analyzer

J. Singh and A. Muller\*

Physics Department, University of South Florida, Tampa, Florida 33620, USA

E-mail: mullera@usf.edu

**Abstract** 

The detection of ambient outdoor trace hydrocarbons was investigated with a multipass

Raman analyzer. It relies on a multimode blue laser diode receiving optical feedback from a

retroreflecting multipass optical cavity, effectively creating an external cavity diode laser

within which spontaneous Raman scattering enhancement occurs. When implemented

with ultralow-loss mirrors, a more than 20-fold increase in signal-to-background ratio was

obtained, enabling proximity detection of trace motor vehicle exhaust gases such as H<sub>2</sub>, CO,

NO,  $CH_4$ ,  $C_2H_2$ ,  $C_2H_4$ , and  $C_2H_6$ . In a 10 min-long measurement at double atmospheric

pressure, the limits of detection obtained were near or below 100 parts-per-billion for most

analytes.

Introduction

Chemical composition analysis is an indispensable necessity in almost all areas of industrial,

medical, and scientific activities. Molecular identification in the gas phase, in particular, is

needed for metrology, product quality control, medical diagnostics, leak detection and envi-

ronmental sensing—on site or via a sample collection process. Often applications are greatly

1

extended by the ability to differentiate between molecular isotopologues, for instance for tracing in environmental or medical diagnostics.

A variety of techniques are capable of trace detection in gases including ion mobility spectrometry (IMS), mass spectrometry, gas chromatography, spin resonance, techniques based on chemically sensitized electromechanical devices, and optical techniques. Among the latter, optical absorption modalities, such as cavity-ring-down spectroscopy (CRDS), 25 have found commercial use for many years. Spontaneous Raman scattering (SRS), on the other hand, has been used commercially for gas sensing only for concentrated analytes. Recently, however, decreasingly lower limits of detection have been reported for gas SRS enhanced by hollow-core optical fibers, <sup>[6-11]</sup> capillaries, <sup>[12]</sup> microcavities, <sup>[13]14]</sup> and multipass cavities. <sup>[15-20]</sup> Besides isotopologue discrimination, a unique advantage of SRS is the ability to sense many gases simultaneously with the same detector and pump source. Numerous recent studies have highlighted this capability. For example, natural gas has been characterized in detail with as many as 7-8 chemicals identified simultaneously. 21122 Pre-mixed samples of hydrocarbons in air have also been characterized successfully, with limit of detection for some hydrocarbons as low as 90 partsper-million (ppm). 23 However, while these efforts constitute a significant step forward in SRS spectroscopy, further improvements are clearly needed to deploy the technique for highly dilute detection at concentrations well below 1 ppm, routinely achieved with competing methods. We report here a step in this direction using a multipass cavity Raman analyzer constructed with ultralow-loss mirrors of reflectivity greater than 99.99%. Compared with off-the-shelf dielectric broadband mirrors with a reflectivity of 99.5%, an average SRS emission rate increase of a factor of 3, together with a background reduction by a factor of 6.5, were obtained. With mild pressurization (0.2 MPa absolute pressure), detection for numerous analytes could be performed at limits of detection near 100 parts-per-billion (ppb) and below in 10 minutes. In particular, a real-world application—the detection of hydrocarbons around a combustion engine motor vehicle exhaust—was possible, simultaneously evidencing an array of trace constituents including H<sub>2</sub>, CO, NO, C<sub>2</sub>H<sub>2</sub>, C<sub>2</sub>H<sub>4</sub>, C<sub>2</sub>H<sub>6</sub>, and CH<sub>4</sub>, bringing SRS sensing into the realm of practical

tools with commercial applications.

#### Context

As a relatively weak light-matter interaction, spontaneous Raman scattering must be enhanced in practice to be useful for trace gas detection. As has been shown in a plethora of recent experiments, there are many ways in which this SRS enhancement can be accomplished. Enhancement mechanisms broadly fall into two categories: (i) cavity assisted enhancement, wherein light is recirculated over a same sample volume, and (ii) waveguide assisted enhancement with light confined tightly over a long channel containing the sample. Advantages and drawbacks of both of these approaches have been reviewed for example by Wang et al. 24 and Knebl et al. 25 Regardless of the enhancement method chosen, in order to identify a trace analyte's spectral signature—typically a Q-branch spectral band—the associated photon flux must significantly exceed the noise in the total photon flux at or near the Stokes frequency. This noise level, although ultimately determined by signal shot noise, is often dominated by the noise in background light, particularly under integration times of minutes or longer. Consequently, a critical step towards lowering the limit of detection in SRS is mitigation of background light generation. In some cases, the background light might be largely due to overlapping secondary SRS emission from other molecules—for example O and S branch bands of nitrogen or oxygen in air—and system spectral selectivity will crucially affect its influence. Fortunately, typical (rotationally-resolved) Raman spectral lines in ambient gases are exceedingly narrow (below 1 cm<sup>-1</sup>). Thus, spectral discrimination is then limited first and foremost by the pump laser linewidth and the detection linewidth, both limited mostly by cost. In other cases, the background will primarily be due to light that is not from other gases' SRS. For such a situation, better spectral selectivity is beneficial, but the residual background will ultimately compromise the ability to identify a spectral line from a particular analyte if the line's magnitude is comparable to the noise in the background.

# **Multipass Cavity**

Multipass cavity SRS enhancement is ideally-suited as an extremely low background light environment. In its simplest form it consists of two concave mirrors in a near-concentric arrangement. This arrangement is well-known and has been used since the early days of laser physics to increase a laser's circulating power without involving a resonance condition, such as is inevitably present in a standing wave or travelling wave resonant cavity. However, due to background mitigation concerns, Raman scattering occurring at the two foci is ordinarily collected sideways. In prior work we have shown that a multipass cavity can be operated in such a way that it serves a triple role of (i) laser power enhancement, (ii) laser feedback generation, and (iii) SRS collection enhancement. [18]20[26] As depicted in Fig. 1, this is possible when the pump rays entering the multipass cavity ultimately retrace their path. Such configuration arises under a slight off-axis alignment of the two concave mirrors and enables a collection path of SRS photons that is collinear with the pump laser path—the two paths being dichroically distinguishable. Details of our setup are provided in Ref. We focus here on the influence of the properties of the multipass cavity mirrors on the overall Raman measurement and show that these constitute a critical factor in realizing trace detection at concentrations below 1 part-permillion.

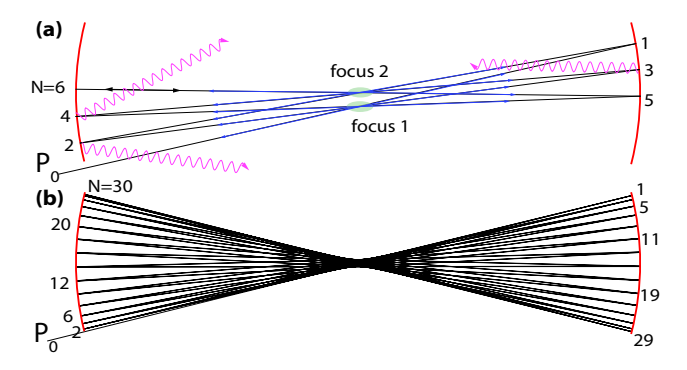


Figure 1: Schematic (a) and raytracing simulation (b) of bidirectional multipass cavity with 2N = 12 and 2N = 60 total mirror reflections, respectively. The pink waves indicate scattering originating from the dielectric coating in the mirrors. The blue arrows indicate the origin and propagation direction of spontaneous Raman scattering which is eventually collected collinearly.

To aid in the analysis, we turn to a simple ray model, illustrated in Fig. 1 wherein a total 2N reflections occur, N being the number of forward reflections. In this model we assume that rays pass alternately through one of two foci and incur a loss of L = 1 - R at each reflection, where R is the mirror power reflectivity coefficient. For simplicity we further assume that rays overlap and combine incoherently at the foci. Thus, we can obtain an expression for the total pump power circulating in the forward direction through focus 1 as

$$P_{\text{pump}_1}^{(\text{FWD})} = P_0 \sum_{n=0}^{\frac{N}{2}-1} R^{2n} = P_0 \frac{1 - R^N}{1 - R^2}$$
 (1)

and that circulating in the backward direction through focus 1 as

$$P_{\text{pump}_1}^{(\text{BKWD})} = P_0 R^{N+1} \sum_{n=0}^{\frac{N}{2}-1} R^{2n} = P_0 R^{N+1} \frac{1 - R^N}{1 - R^2}.$$
 (2)

Likewise, for the second focus, the powers are

$$P_{\text{pump}_2}^{(\text{FWD})} = RP_0 \sum_{n=0}^{\frac{N}{2}-1} R^{2n} = RP_0 \frac{1 - R^N}{1 - R^2}$$
 (3)

and

$$P_{\text{pump}_2}^{(\text{BKWD})} = P_0 R^N \sum_{n=0}^{\frac{N}{2}-1} R^{2n} = P_0 R^N \frac{1 - R^N}{1 - R^2}.$$
 (4)

Forward and backward Raman scattering is assumed to occur into each reflection direction from each focus with proportionality constant  $\alpha$  to the pump power. Specifically,

$$P_{SRS_1}^{(FWD)} = \alpha \left( P_{pump_1}^{(FWD)} + P_{pump_1}^{(BKWD)} \right) R^{N+1} \frac{1 - R^N}{1 - R^2},$$
 (5)

$$P_{SRS_1}^{(BKWD)} = \alpha \left( P_{pump_1}^{(FWD)} + P_{pump_1}^{(BKWD)} \right) \frac{1 - R^N}{1 - R^2},$$
 (6)

$$P_{SRS_2}^{(FWD)} = \alpha \left( P_{pump_2}^{(FWD)} + P_{pump_2}^{(BKWD)} \right) R^N \frac{1 - R^N}{1 - R^2},$$
(7)

and

$$P_{SRS_2}^{(BKWD)} = \alpha \left( P_{pump_2}^{(FWD)} + P_{pump_2}^{(BKWD)} \right) R \frac{1 - R^N}{1 - R^2},$$
 (8)

so that the total collected SRS rate is

$$P_{SRS} = P_{SRS_1}^{(FWD)} + P_{SRS_1}^{(BKWD)} + P_{SRS_2}^{(FWD)} + P_{SRS_2}^{(BKWD)}.$$
 (9)

The quantity  $\frac{P_{SRS}}{\alpha P_0}$  represents the multipass cavity enhancement factor, i.e., the ratio of the total SRS emission with the multipass cavity to the SRS emission that would be measured if the multipass cavity were removed. Despite the crude simplifications made in the model, it provides insight into the influence of mirror properties on the overall SRS enhancement. In the com-

Table 1: Nominal multipass enhancement factor  $\frac{P_{SRS}}{\alpha P_0}$  for two sets of curved mirrors, for different number of one-way reflections N. The stated reflectivities are nominal for  $\lambda$  =445 nm (near pump wavelength) and  $\lambda$  =510 nm (methane Stokes wavelength) as stated by the manufacturer. The experimental enhancement factor is relative to the one obtained with off-the-shelf dielectric mirrors (Thorlabs CM254-025-E02).

| Mirrors                | $R_{445nm}$ | $R_{510nm}$ | Nominal $\frac{P_{SRS}}{\alpha P_0}$ |        |        | Rel. exp. $\frac{P_{SRS}}{\alpha P_0}$ |
|------------------------|-------------|-------------|--------------------------------------|--------|--------|--|
|                        | (%)         | (%)         | N = 20                               | N = 30 | N = 40 | N = 30                                 |
| Thorlabs CM254-025-E02 | 99.8        | 99.0        | 640                                  | 1280   | 2040   | 1                                      |
| Layertec 20030278      | 99.995      | 99.995      | 800                                  | 1800   | 3200   | 2.1                                    |

plete absence of reflection losses, i.e., when  $R \to 1$ , we get  $\frac{1-R^N}{1-R^2} \to \frac{N}{2}$  and thus  $P_{SRS} = 2\alpha P_0 N^2$ , i.e., a superlinear growth of the SRS rate with the number of reflections occurs. Thus, there is significant benefit in maximizing N, as well as R. While N is largely determined by the ratio of the solid angle subtended by the cavity mirrors to that of the incoming beam, the reflectivity of ordinary broadband dielectric mirrors typically does not exceed 99.5%. However, ultralow loss mirrors can be manufactured by ion beam sputtering with reflectivities routinely above 99.99% such that in practice essentially no reflective losses are incurred. Table 1 provides a summary of the nominal SRS multipass cavity enhancement factors,  $\frac{P_{SRS}}{\alpha P_0}$ , theoretically expected based on different sets of mirrors. For the scenario pertinent to our experimental setup,  $N \approx 30$ , and the multipass enhancement factor with ultralow loss mirrors is twice the enhancement factor ob-

tained using ordinary dielectric mirrors. The model thus gives a reasonable picture of the losses. Independent reflectivity measurements of the CM254-025-E02 mirrors also show that the real mirror reflectivity is lower than the nominal value provided by the manufacturer, probably due to intrinsic variations in the manufacturing process.

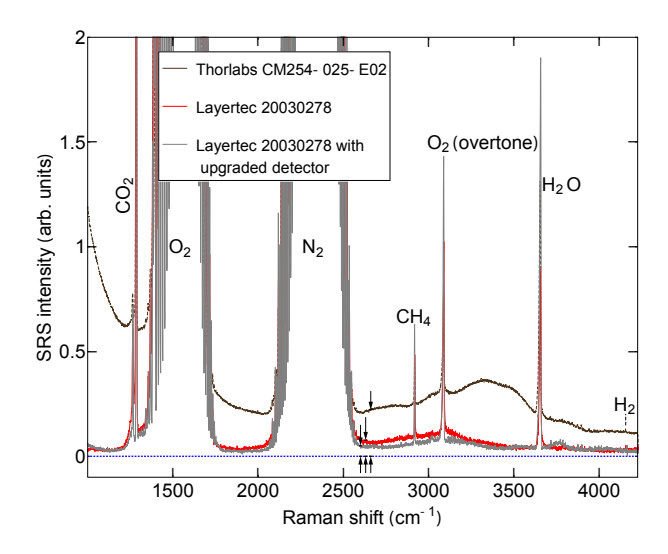


Figure 2: Raman spectra of dried room air obtained with a multipass cavity constructed using commercial off-the-shelf mirrors (dark-brown, Thorlabs CM254-025-E02), ultralow-loss custom mirrors (red, Layertec 20030278), and ultralow-loss mirrors with an upgraded detector (gray). Mirror specifications are provided in Table 1. The exposure time was 60 seconds except for the CM254-025-E02 trace for which the exposure time was 600 s before normalization to 60 s. The pressure was 0.1 MPa. The arrows indicate the midrange background magnitude for the different configurations.

Furthermore, since losses of ordinary broadband mirrors are usually dominated by scattering losses associated with material microroughness, substantial stray light is generated in a multipass cavity built with such mirrors. The stray light is likely generated in the form of diffuse fluorescence and/or spontaneous Raman scattering from surrounding material surfaces which receive the monochromatic pump light scattered by the mirrors. Thus the consequence of this scattering is broadband background light in the SRS spectrum as seen in Fig. 2 for ambient air spectra recorded with cavities built with either ordinary or ultralow loss mirrors. Extracting the signal, background, and signal-to-background magnitude ratios at two different spectral locations from the data of Fig. 2 we obtain the data of Table 2. As can be seen, the combined

effect of reduced losses and reduced scattering lead to an average 24-fold increase in signal-to-background ratio between the two mirror sets. If an improved spectrometer is used (gray trace in Fig. 2), then the overall increase in signal-to-background ratio is 30-fold (overall spectral resolution of  $<3.5~\rm cm^{-1}$ ). The arrows in Fig. 2 indicate the midrange background magnitude for the different configurations.

Table 2: Relative signal, background, and signal-to-background magnitude ratio of ambient air SRS spectra recorded with a multipass cavity build with different sets of curved mirrors. The two spectral locations correspond to ambient carbon dioxide (1285 cm<sup>-1</sup>) and methane (2917 cm<sup>-1</sup>).

| Mirrors                    | Rel. magn. $(1285 \text{ cm}^{-1})$ |       |              | Rel. magn. $(2917 \text{ cm}^{-1})$ |       |              |
|----------------------------|-------------------------------------|-------|--------------|-------------------------------------|-------|--------------|
|                            | signal                              | bkgnd | signal/bkgnd | signal                              | bkgnd | signal/bkgnd |
| Thorlabs CM254-025-E02     | 1                                   | 0.34  | 2.94         | 1                                   | 1.59  | 0.63         |
| Layertec 20030278          | 3.93                                | 0.03  | 131          | 2.06                                | 0.77  | 2.68         |
| Layertec+upgraded detector | 4.78                                | 0.03  | 159          | 3.29                                | 0.41  | 8.02         |

## Trace sensing in a practical setting

Because the noise in our measurements is dominated by background shot noise, as opposed to camera read noise or signal shot noise, a reduced signal-to-background ratio makes it possible to significantly lower the limit of detection for most molecules. As a test application, hydrocarbon residuals in air were analyzed. Outdoor air samples were collected behind a motor vehicle equipped with a 2.5 L, 4 cylinder gasoline engine. The vehicle was stationary and idling at around 900 revolutions per minute. The sample was pressurized to near 0.2 MPa with a hand pump into a plastic container with a volume of 3.7 L, and subsequently transported to the laboratory where it was introduced into a partially evacuated chamber ( $\approx$ 0.02 MPa) enclosing the SRS multipass cavity. The delay between collection and measurement was about 5 minutes.

Auxiliary procedures and experimental settings were similar to those adopted in prior work. The multimode laser diode pump source (Nichia NUBM44) was operated at a current of 1.8 A and a temperature of 23°C, conditions under which it would produce a free running output power of 2.4 W at a wavelength of 443 nm. The volume Bragg grating by which frequency-

selective feedback is obtained reduces the laser linewidth to approximately 3 cm $^{-1}$ . The spectral detection system was improved over prior work in terms of efficiency and resolution. With an input numerical aperture of 0.22 and slit width of 50  $\mu$ m, it was optimized to match better the multipass light collection optics. The chamber holding the multipass cavity was systematically operated at an absolute pressure of 0.2 MPa. Spectral calibration was preformed using known Raman shifts associated with ambient air molecules such as water vapor. Recordings were segmented into five 2-min-long exposures using a CMOS detector (SONY IMX183 in ZWO ASI183 mono camera) without gain to maximize dynamic range.

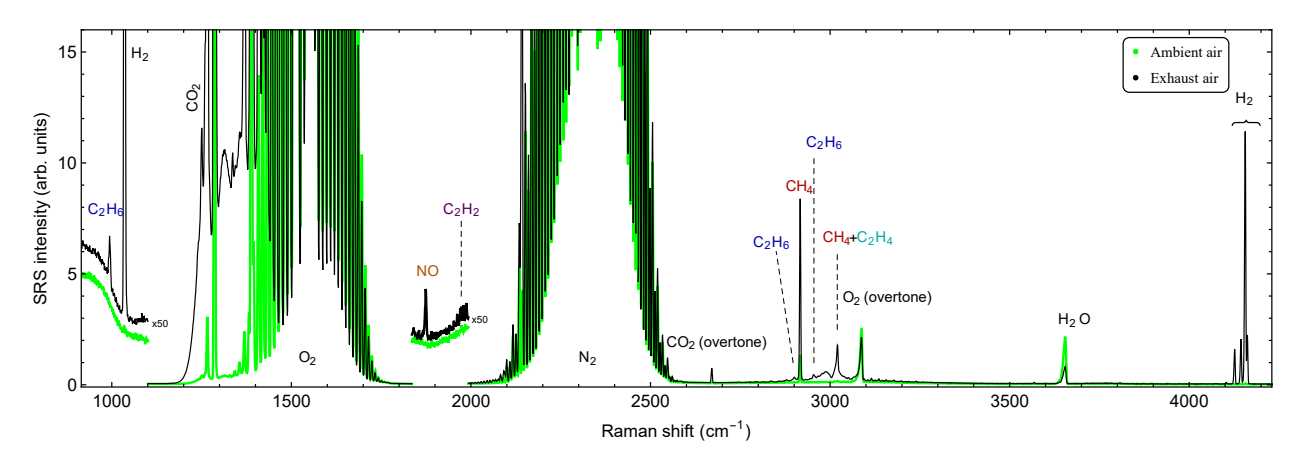


Figure 3: [Two-column] Overview of Raman spectra of dried ambient (green) and exhaust air (black) at a pressure of 0.2 MPa. A typical sample of exhaust air is rich in carbon dioxide, carbon monoxide, nitric oxide, hydrogen and aliphatic hydrocarbons like methane, ethane, acetylene and ethylene. A magnified view (×50) was applied to selected spectral regions for better visualization.

Raman spectra were first recorded for samples collected about 0.1 m away from the exhaust outlet and subsequently dried with desiccant. The removal of water vapor—and its many O-H stretching and O-H bending spectral features—facilitates spectral interpretation but is not strictly necessary. Although much sample-to-sample variability is observed due to the nature of our crude sampling method, most exhaust gas spectra resemble the spectrum shown in Fig. 3 (gray trace) with a large number of peaks that are not seen in spectra from ambient air (green trace in Fig. 3). In order of characteristic abundance these are Q-branch bands of  $CO_2$ , CO,  $H_2$ ,  $CH_4$ ,  $C_2H_4$ ,  $C_2H_6$ , NO, and  $C_2H_2$ , as summarized in Table 3. The Q-branch bands of isotopo-

Table 3: Spectral bands of gases detected in dried gasoline engine exhaust air. The differential Raman scattering cross section  $d\sigma/d\Omega$  is specified relative to that of  $N_2$  at a pump wavelength of 443 nm. The last two columns display the lowest measured concentration, and the limit of detection (LOD) for each analyte, respectively. We define the LOD as the concentration at which the signal to noise ratio equals five during a 10 minute long acquisition.

| Gas          | Symbol           | $\bar{\nu}_R$      | $mode^a$                   | $d\sigma/d\Omega$  | Min. conc.   | LOD   |
|--------------|------------------|--------------------|----------------------------|--------------------|--------------|-------|
|              |                  | $(cm^{-1})$        |                            |                    | (ppb)        | (ppb) |
| Hydrogen     | $H_2$            | 4155 <sup>29</sup> | H–H str.                   | $2.62^{30b}$       | $680^{31}d$  | 100   |
| Nitric oxide | NO               | 1875 <sup>30</sup> | N–O str.                   | $0.35^{30}$        | 420          | 330   |
| Methane      | $\mathrm{CH}_4$  | $2917^{32}$        | C–H str.                   | $7.6^{30}$         | $1900^{33}d$ | 20    |
|              | $\mathrm{CH}_4$  | $3017^{32}$        | C–H bend                   | $0.21^{3032}$      |              |       |
| Ethane       | $C_2H_6$         | 2955 <sup>34</sup> | C–H str.                   | $9.56^{32}$        | 60           | 20    |
|              |                  | $2900^{34}$        | C–H str.                   | $5.08^{32}$        |              |       |
|              |                  | $2745^{34}$        | $2 \times CH_3$ sciss.     | $0.80^{3032}$      |              |       |
|              |                  | $993^{30 34}$      | C–C str.                   | $2.2^{3032}$       |              |       |
| Ethylene     | $C_2H_4$         | $3020^{30}$        | C–H str.                   | $5.57^{30}$        | 370          | 80    |
|              |                  | $2880^{30}$        | C–H str.                   | $0.14^{3032}$      |              |       |
| Acetylene    | $C_2H_2$         | 1973 <sup>30</sup> | C–C str.                   | $8.55^{30}$        | 30           | 20    |
| Carb. monox. | $^{12}C^{16}O$   | $2142^{30}$        | C–O str.                   | $0.89^{30}$        |              |       |
|              | $^{13}C^{16}O$   | $2095^{35}$        | C–O str.                   | -                  |              |       |
| Carb. diox.  | $^{12}C^{16}O_2$ | 1388 <sup>30</sup> | C–O str.+bend <sup>c</sup> | 1.33 <sup>30</sup> |              |       |
|              | $^{13}C^{16}O_2$ | 1370 <sup>36</sup> | C–O str.+bend <sup>c</sup> | -                  |              |       |

a"str.", "bend", and "sciss." stand for stretching, bending and scissoring vibration, respectively, and overtones are labelled with "2×". bSum of all rotationally-resolved transitions.  $v_+$  transition in the Fermi Dyad. dAmbient level.

logues  $^{13}C^{16}O_2$  and  $^{13}C^{16}O$  are also identified. For the most abundant species, e.g.,  $CO_2$ ,  $H_2$ ,  $CH_4$  and CO, series of peaks associated with O and S branch transitions are seen as well. To demonstrate unequivocal chemical identification and accurate assessment of concentrations we look more closely at the spectral region corresponding to C-H stretching vibrations (Fig. 4). It is dominated by bands due to methane. However, upon careful inspection, it is possible to identify bands associated with  $CO_2$ ,  $C_2$ ,  $C_2$ ,  $C_4$ , and  $C_4$ . This is clear from the "pure" gas spectra of methane, oxygen, and carbon dioxide, overlaid with the exhaust gas spectrum in Fig. 4(a), where the spectra have been scaled according to their relative estimated concentrations. We can further create a "synthetic spectrum" composed of spectra of the pure gases and generate a "reduced" exhaust gas spectrum by subtraction, as seen in Fig. 4(b). It is then evident that the remaining peaks belong to the less abundant species of  $C_2H_4$  and  $C_2H_6$ , which is confirmed

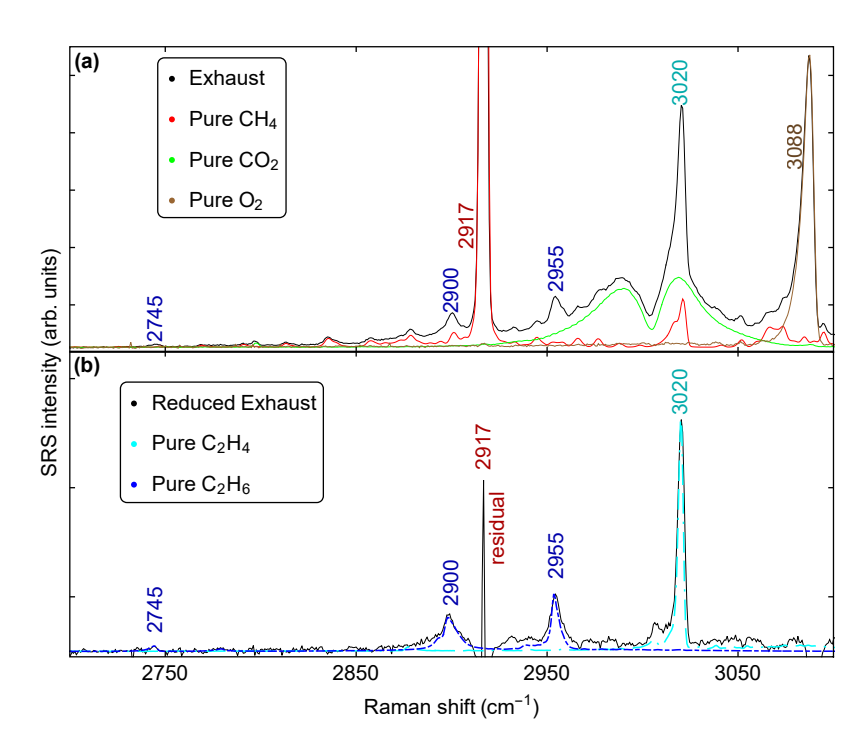


Figure 4: [Two-column] Magnified view of Fig. 3 C-H stretching region. (a) Spectra of exhaust gas, pure methane, pure oxygen and pure carbon dioxide. (b) Exhaust gas spectrum from which the sum of pure gas spectra from (a) was subtracted, together with ethane and ethylene spectra from Magnotti et al. [32]

upon plotting the spectra of pure  $C_2H_4$  and pure  $C_2H_6$  together with the reduced exhaust spectrum in Fig. 4(b). At lower frequencies, C–C stretching vibrations give rise to a peak from  $C_2H_2$ , which is more or less isolated depending on the magnitude of the overlapping O-branch band due to carbon monoxide. In Fig. 5, a magnified view of this spectral feature is shown for three different exhaust samples. As can be seen, substantial concentration variations occur, presumably due to variations in engine operation. In some cases, for example for sample 2, the peak associated with  $C_2H_2$  at 1973 cm<sup>-1</sup> can only barely be identified. In this particular sample, carbon monoxide content was particularly high so that the Q-branch SRS feature due to  $^{13}C^{16}O$  near 2095 cm<sup>-1</sup> is also detected as indicated in Fig. 5. Many of the spectral features identified above are still visible at lower concentrations. To illustrate this, samples were collected at farther distances of 0.75 m and 1.25 m from the exhaust outlet. In Fig. 6, we can see for instance that up to a distance of 0.75 m from the outlet, ethane and nitric oxide remain barely detectable. Hydrogen remains detectable at distances over 1 m, i.e., the magnitude of peaks shown in Fig.

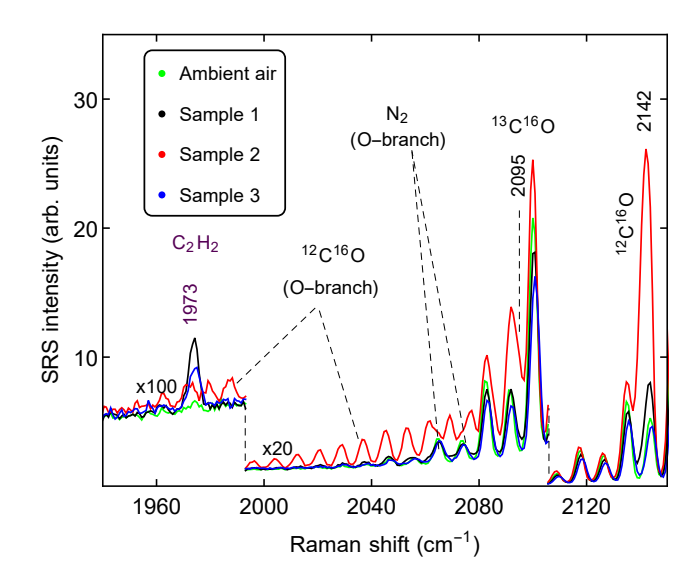


Figure 5: Spectral Q-branch line due to acetylene  $(C_2H_2)$  at 1973 cm<sup>-1</sup> at the tail of O-branch lines from  $^{12}C^{16}O$  and/or  $N_2$  for 3 different samples of exhaust air, and for ambient air.

6(c) for the collection distance of 1.25 m still significantly exceeds that of the peaks recorded for ambient air, for which the hydrogen concentration is about 0.7 ppm. Likewise, we can observe in the spectra of Fig. 7 that ethylene, despite having a spectral signature in a region shared with, in particular, carbon dioxide SRS, remains detected at a distance of 0.75 m. These measurements demonstrate that even under extreme dilution trace residuals from the combustion are still measurable. We can estimate the concentrations of the molecular species tabulated in table 3 based on peak magnitudes and known cross sections, also listed in table 3. Here we primarily utilize ambient methane (1.9 ppm) as the reference for the concentration of aliphatic hydrocarbons in the spectral range around 3000 cm<sup>-1</sup>, as well as for nitric oxide. For hydrogen, we compare directly with measurements on a calibrated reference gas for which the hydrogen concentration is certified as 2 ppm (Airgas part number X02AI99C15A48N1). The results are summarized in Fig. 8 as a function of the collection distance from the outlet. As can be seen in Fig. 8, hydrocarbons are detected at concentrations ranging from ~2 ppm down to ~0.03 ppm. Several species such as C<sub>2</sub>H<sub>2</sub> and C<sub>2</sub>H<sub>6</sub> were measured at concentrations as low as 50 partsper-billion (ppb), thanks to exceptionally large scattering cross sections. Nitric oxide, due to the high degree of spectral isolation of its Q-branch peak, was measured as low as 420 ppb. The

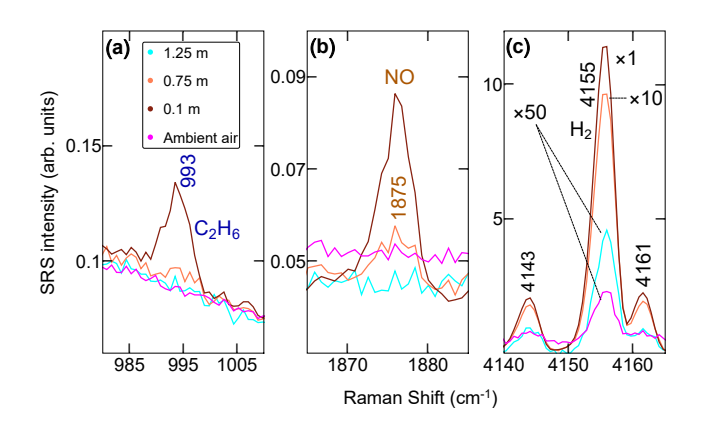


Figure 6: SRS spectra centered around the peaks associated with ethane (a), nitric oxide (b), and hydrogen (c), for exhaust gas samples collected at different distances to the outlet.

lowest concentrations measured for each analyte are listed in the next to last column of table 3.

Nevertheless, lower concentrations than those present in the measurements of Fig. 6 and Fig. 7 are potentially detectable. To assess the limit of detection (LOD) for each species realistically, we extract the noise level, i.e., the root mean square background fluctuation in the vicinity of its associated spectral peak. We define the LOD as the concentration at which the peak area is five times the integrated noise level in the total recording time of 10 minutes. The results are tabulated in the last column of table 3. For those analytes with the largest cross sections, exceptionally low LODs of order 20 ppb are found. That these LOD numbers provide a conservative measure of the lowest detectable concentration is demonstrated from a comparison with the actually detected concentrations. For example, the spectral feature for acetylene in Fig. 5 in the blue trace belonging to sample 3 (estimated concentration of 30 ppb) would most certainly still be visible with a further reduced concentration (LOD of 20 ppb). Likewise, the orange trace in Fig. 6(b) representing NO at an estimated 420 ppb is intuitively close to the LOD estimated at 330 ppb (LODs have been rounded up to the nearest 10 ppb).

To formally verify the validity of the LOD figures obtained, a series of concentration-dependent measurements was performed for methane. Ambient air containing  $CH_4$  at a concentration of 1.9 ppm was diluted in  $N_2$  (ultra-high purity nitrogen from Airgas) so as to vary the methane concentration in steps of approximately 10 ppb. The SRS spectrum was measured for each con-

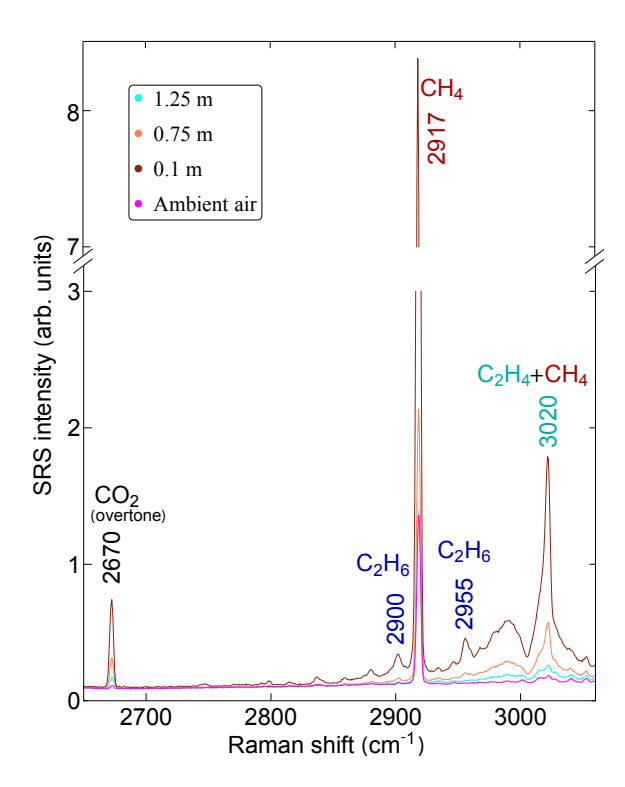


Figure 7: SRS spectra in the C-H stretching region for exhaust gas samples collected at different distances to the outlet.

centration under the same conditions as those of the exhaust gas measurements above (10 min measurement time at 0.2 MPa absolute pressure). The results are summarized in Fig. 9. In part (a) spectra at selected concentrations are displayed, whereas in part (b) the signal magnitude (peak height) is plotted relative to the noise magnitude (SNR), as a function of methane concentration. As can be seen, the methane spectral signature at 2917 cm<sup>-1</sup> is buried in the noise for concentrations below about 20 ppb, in agreement with the LOD reported in table 3.

#### **Discussion**

Today more than ever, trace chemical concentration analysis in air is crucial for a wide variety of applications. The results above show that Raman scattering has potential as an alternative trace gas detection method in the ppb range. Depending on the particular analyte being measured, there could be room for improvement beyond using ultralow loss mirrors. For all data presented here, the limiting noise remains random background noise. Unless the background

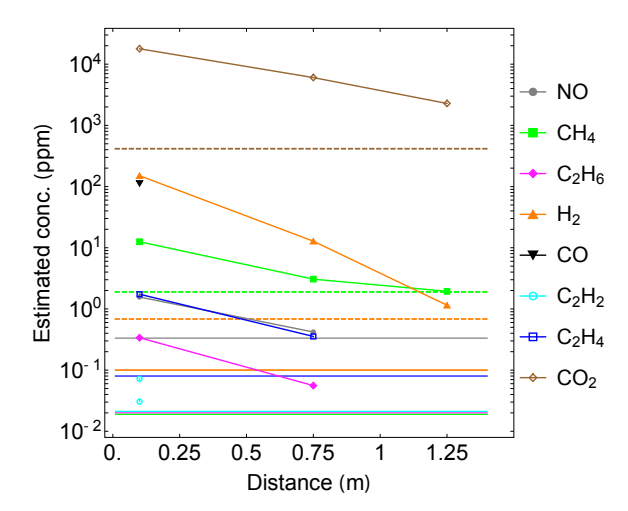


Figure 8: Summary of estimated concentrations of analytes in the measurements of Fig. 6 and Fig. 7 for various distances between sample collection and exhaust outlet. For  $C_2H_2$  we show two measurements at 0.1 m distance to illustrate variability among repeated measurements. The dashed lines indicate the ambient levels for selected gases, and the solid lines show the limits of detection as listed in Table 3. The distance indicated effectively carries a relatively large uncertainty estimated at ~10 cm due to the nature of the uncontrolled sampling method employed.

is produced by other analytes' SRS, it should be possible to realize measurements for which camera read noise dominates under short exposure times, and signal shot noise dominates under long exposure times. Attaining this regime will be most likely limited by cost of components since there is a priori no reason to assume that stray light emerging from locations exterior to the sample volume cannot be discriminated, albeit at a potential loss in efficiency. Simple and versatile detection at order 10 to 100 ppb could open up new applications for Raman scattering, heretofore covered primarily by more established and relatively expensive techniques. Below we provide a brief summary of potential impacts.

Ethane— Ethane ( $C_2H_6$ ) is a hydrocarbon with a rapidly increasing atmospheric concentration due to underground fossil fuel extraction. Although the global average atmospheric concentration of ethane is only of order 1 ppb, it has been estimated to increase by 5% each year. In addition, local concentrations can be much greater, for instance near gas processing plants. Ethane serves as a tracer for methane because of the nearly nonexistent non-fossil fraction of ethane in air. Thus there could be considerable interest in the development of pre-

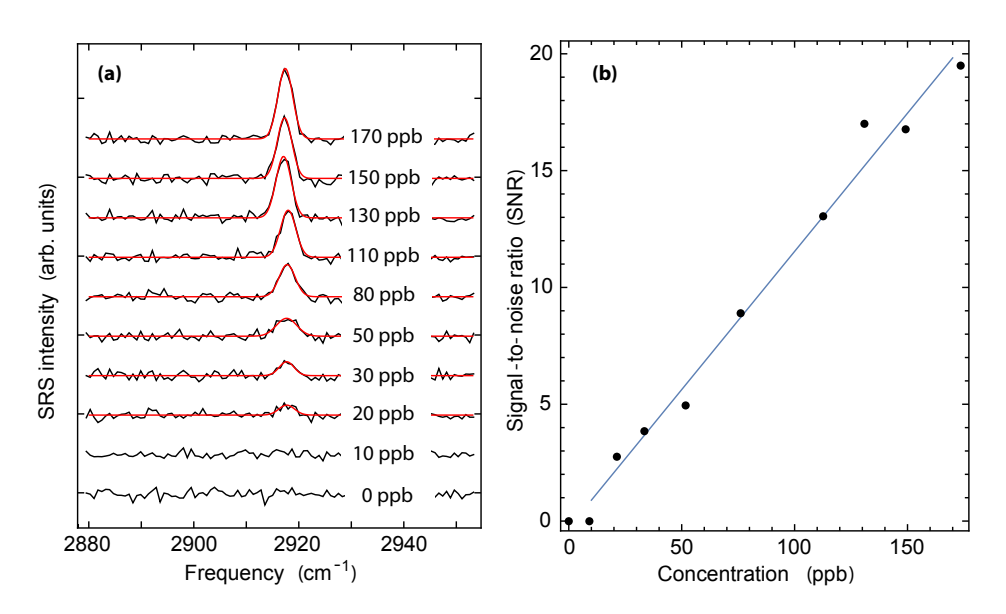


Figure 9: (a) [Two-column] SRS spectra of methane for concentrations indicated, offset vertically for clarity. (b) Signal-to-noise ratio as a function of concentration. The SRS signal intensity was obtained as the peak heights in part (a), whereas the (concentration-invariant) noise level was extracted as the root-mean-square baseline variation in the peak vicinity.

cise and robust ethane trace sensors. Currently, infrared absorption techniques are nearly able to reach detection of ambient levels of ethane. For example, commercial cavity ring down detectors have been shown to be sensitive to changes in ethane concentration of order 10 ppb. Nonetheless, an analyzer based on Raman scattering could bring advantages due to potentially lower cost associated with the ability to co-detect a host of other molecular species simultaneously.

Ethylene—Besides being widely employed in the manufacturing of plastics, ethylene ( $C_2H_4$ ) serves as an important hormone in plants, and real time monitoring systems for ethylene have applications in agriculture, horticulture and health care. Ethylene is synthesized by plants themselves and active at concentrations of tens of ppb to one ppm. Thus trace ethylene gas concentration monitoring is relevant for instance in fruit ripening systems. Studies with hollow core fiber enhancement have already demonstrated the suitability of Raman scattering for this task. Measurements were performed down to concentrations of 100 ppm when employing the spectral feature at 1342 cm<sup>-1</sup> for ethylene identification. This band is spectrally overlapping with  $CO_2$  SRS, thus hindering substantially the detection at levels below 1 ppm. The exception-

ally low background concentrations available in multipass cavity enhanced Raman scattering in the C-H stretching region allows to detect ethylene at the 3020 cm<sup>-1</sup> peak instead, which is also associated with a greater cross section (by approximately a factor of two). The lowest  $C_2H_4$  concentration detected in our studies was 370 ppb and we estimate the limit of detection to be 80 ppb. Detecting ethylene at that level in the context of monitoring fruit ripening should be substantially easier compared to the monitoring of ethylene in gasoline exhaust gases: the 3020 cm<sup>-1</sup> ethylene peak happens to nearly overlap with the 3017 cm<sup>-1</sup> methane peak, as well as with a wide band due to  $CO_2$ , both abundant in exhaust gases (see Fig. 4).

Acetylene—Acetylene ( $C_2H_2$ ) finds use predominantly in metallurgy for welding. It is also used as a precursor in the production of, e.g., plastics. The simplest alkyne, it is characterized by a Raman scattering cross section greater than even that of methane. Its triple bond C-C stretching vibration frequency lies well isolated from those of other common hydrocarbons and acetylene is therefore highly detectable by Raman scattering, with an estimated limit of detection of 20 ppb in our study. Safety monitoring in industrial process control could potentially benefit from such high detectability. Acetylene is also present in the breath of smokers at concentrations as high as 260 ppb,  $^{42}$  but fast elimination in exhaled breath does not make it an efficient biomarker for active smokers.  $^{43}$ 

Nitric oxide—Together with other oxides of nitrogen, nitric oxide (NO) is a major pollutant on roadways. Diesel vehicles in particular generate significant amounts of nitric oxide. Near roadways, nitric oxide concentrations can reach concentrations well in excess of 10 ppb. [44] Nitric oxide is also a chemical messenger in the human body. It is normally found in breath at concentrations near 200 ppb, and NO deficiencies have been linked to a variety of diseases. [45] Given an estimated LOD of 330 ppb in our present study with 10-min long recording times, it appears feasible to reach NO detectability near 100 ppb. For example, this could simply be achieved by moderate increases in laser pump power and exposure times, thus enabling medical diagnostics applications.

Hydrogen—Despite being the most abundant element in the universe, the atmospheric concentration of hydrogen gas (H<sub>2</sub>) is only about 0.7 ppm. As a homonuclear diatomic molecule, hydrogen is difficult to detect with infrared absorption. Nevertheless, the need for precise and reliable hydrogen gas detection devices has never been greater, due in part to the burgeoning hydrogen energy industry. Hydrogen detection systems are being researched extensively and sensors relying on chemically sensitized metal oxide semiconductors (MOS) devices are particularly promising. However, a major advantage of SRS hydrogen gas sensors over MOS sensors is improved accuracy at detection levels of order 10 ppb at room temperature. Hydrogen also plays a major role in atmospheric science and could find use in leak detection systems to replace or complement expensive Helium based tools. Finally, in the context of medical applications, hydrogen detection is at the heart of the hydrogen breath test. For this test, hydrogen gas concentrations very near ambient concentrations (order 1 ppm) need to be assessed precisely.

### **Conclusions**

In summary, the utilization of ultra-low loss mirrors (reflectivity greater than 99.99%) in a multipass cavity laser feedback configuration has enabled spontaneous Raman scattering measurements subject to exceptionally low background and increased signal intensity. With correspondingly suppressed noise, detection at previously unreachable trace concentrations was possible. Limits of detection for NO,  $H_2$ ,  $C_2H_2$ ,  $C_2H_4$ , and  $C_2H_6$ , where obtained as 330 ppb, 100 ppb, 20 ppb, 80 ppb, 20 ppb, respectively, at an exposure time of 10 min, which potentially enables a variety of new applications for SRS. Importantly this was achieved with an ordinary multimode laser diode as the pump source, with high potential for portability. Given that most SRS trace gas sensing approaches employ highly pressurized gas samples it is likely that significant improvements can be made by simply operating in a higher pressure environment, conceivably reaching detection limits of order 1 ppb for some analytes.

## Acknowledgement

The authors acknowledge the financial support from the National Science Foundation (NSF grant No. 2116275).

### References

- (1) Moore, D. S. Instrumentation for trace detection of high explosives. *Rev. Sci. Instrum.* **2004**, 75, 2499–2512.
- (2) Galewsky, J.; Steen-Larsen, H. C.; Field, R. D.; Worden, J.; Risi, C.; Schneider, M. Stable isotopes in atmospheric water vapor and applications to the hydrologic cycle. *Rev. Geophys.* **2016**, *54*, 809–865.
- (3) Ciaffoni, L.; Hancock, G.; Harrison, J. J.; van Helden, J.-P. H.; Langley, C. E.; Peverall, R.; Ritchie, G. A.; Wood, S. Demonstration of a mid-infrared cavity enhanced absorption spectrometer for breath acetone detection. *Anal. Chem.* **2013**, *85*, 846–850.
- (4) Wang, J.; Tian, X.; Dong, Y.; Zhu, G.; Chen, J.; Tan, T.; Liu, K.; Chen, W.; Gao, X. Enhancing off-axis integrated cavity output spectroscopy (OA-ICOS) with radio frequency white noise for gas sensing. *Opt. Express* **2019**, *27*, 30517–30529.
- (5) Van Helden, J.; Lang, N.; Macherius, U.; Zimmermann, H.; Röpcke, J. Sensitive trace gas detection with cavity enhanced absorption spectroscopy using a continuous wave external-cavity quantum cascade laser. *Appl. Phys. Lett.* **2013**, *103*, 131114.
- (6) Hanf, S.; Keiner, R.; Yan, D.; Popp, J.; Frosch, T. Fiber-enhanced Raman multigas spectroscopy: a versatile tool for environmental gas sensing and breath analysis. *Anal. Chem.* 2014, 86, 5278–5285.
- (7) Hanf, S.; Bogozi, T.; Keiner, R.; Frosch, T.; Popp, J. Fast and highly sensitive fiber-enhanced

- Raman spectroscopic monitoring of molecular H2 and CH4 for point-of-care diagnosis of malabsorption disorders in exhaled human breath. *Anal. Chem.* **2015**, *87*, 982–988.
- (8) Yan, D.; Popp, J.; Pletz, M. W.; Frosch, T. Highly sensitive broadband Raman sensing of antibiotics in step-index hollow-core photonic crystal fibers. *Acs Photonics* **2017**, *4*, 138–145.
- (9) Trabold, B. M.; Hupfer, R. J.; Abdolvand, A.; Russell, P. S. J. Broadband high-resolution multi-species CARS in gas-filled hollow-core photonic crystal fiber. *Opt. Lett.* **2017**, *42*, 3283–3286.
- (10) Chu, Q.; Jin, Z.; Yu, X.; Li, C.; Zhang, W.; Ji, W.; Lin, B.; Shum, P. P.; Zhang, X.; Wang, G. Volumetric enhancement of Raman scattering for fast detection based on a silver-lined hollow-core fiber. *Opt. Express* **2019**, *27*, 10370–10382.
- (11) Beffara, F.; Humbert, G.; Auguste, J.-L.; Perumal, J.; Dinish, U.; Olivo, M. Optimization and performance analysis of SERS-active suspended core photonic crystal fibers. *Opt. Express* **2020**, *28*, 23609–23619.
- (12) Pearman, W. F.; Carter, J. C.; Angel, S. M.; Chan, J. W. Quantitative measurements of CO2 and CH4 using a multipass Raman capillary cell. *Appl. Opt.* **2008**, *47*, 4627–4632.
- (13) Petrak, B.; Djeu, N.; Muller, A. Purcell-enhanced Raman scattering from atmospheric gases in a high-finesse microcavity. *Phys. Rev. A* **2014**, *89*, 023811.
- (14) Petrak, B.; Cooper, J.; Konthasinghe, K.; Peiris, M.; Djeu, N.; Hopkins, A.; Muller, A. Isotopic gas analysis through Purcell cavity enhanced Raman scattering. *Appl. Phys. Lett.* **2016**, *108*, 091107.
- (15) Hill, R.; Mulac, A.; Hackett, C. Retroreflecting multipass cell for Raman scattering. *Appl. Opt.* **1977**, *16*, 2004–2006.

- (16) Li, X.; Xia, Y.; Zhan, L.; Huang, J. Near-confocal cavity-enhanced Raman spectroscopy for multitrace-gas detection. *Opt. Lett.* **2008**, *33*, 2143–2145.
- (17) Petrov, D. V. Multipass optical system for a Raman gas spectrometer. *Appl. Opt.* **2016**, *55*, 9521–9525.
- (18) Velez, J. G.; Muller, A. Trace gas sensing using diode-pumped collinearly detected spontaneous Raman scattering enhanced by a multipass cell. *Opt. Lett.* **2020**, *45*, 133–136.
- (19) Velez, J. S. G.; Muller, A. Spontaneous Raman scattering at trace gas concentrations with a pressurized external multipass cavity. *Meas. Sci. Technol.* **2021**, *32*, 045501.
- (20) Singh, J.; Muller, A. Isotopic trace analysis of water vapor with multipass cavity Raman scattering. *Analyst* **2021**, *146*, 6482–6489.
- (21) Khannanov, M. N.; Van'kov, A. B.; Novikov, A. A.; Semenov, A. P.; Gushchin, P. A.; Gubarev, S. I.; Kirpichev, V. E.; Morozova, E. N.; Kulik, L. V.; Kukushkin, I. V. Analysis of natural gas using a portable hollow-core photonic crystal coupled Raman spectrometer. *J. Appl. Spectrosc.* **2020**, *74*, 1496–1504.
- (22) Hippler, M. Cavity-enhanced Raman spectroscopy of natural gas with optical feedback cwdiode lasers. *Anal. Chem.* **2015**, *87*, 7803–7809.
- (23) Knebl, A.; Domes, C.; Domes, R.; Wolf, S.; Popp, J.; Frosch, T. Hydrogen and C2–C6 Alkane Sensing in Complex Fuel Gas Mixtures with Fiber-Enhanced Raman Spectroscopy. *Anal. Chem.* **2021**, 93, 10546–10552.
- (24) Wang, P.; Chen, W.; Wan, F.; Wang, J.; Hu, J. A review of cavity-enhanced Raman spectroscopy as a gas sensing method. *J. Appl. Spectrosc. Reviews* **2020**, *55*, 393–417.
- (25) Knebl, A.; Yan, D.; Popp, J.; Frosch, T. Fiber enhanced Raman gas spectroscopy. *Trends in Anal. Chem.* **2018**, *103*, 230–238.

- (26) Velez, J. S. G.; Muller, A. Spontaneous Raman scattering at trace gas concentrations with a pressurized external multipass cavity. *Meas. Sci. Technol.* **2021**, *32*, 045501.
- (27) Avila, G.; Fernández, J.; Tejeda, G.; Montero, S. The Raman spectra and cross-sections of H2O, D2O, and HDO in the OH/OD stretching regions. *J. Mol. Spectrosc.* **2004**, *228*, 38 65.
- (28) Avila, G.; Tejeda, G.; Fernandez, J.; Montero, S. The Raman spectra and cross-sections of the v2 band of H2O, D2O, and HDO. *J. Mol. Spectrosc.* **2004**, *223*, 166–180.
- (29) Veirs, D. K.; Rosenblatt, G. M. Raman line positions in molecular hydrogen: H2, HD, HT, D2, DT, and T2. *J. Mol. Spectrosc.* **1987**, *121*, 401–419.
- (30) Schrötter, H.; Klöckner, H. In *Raman Spectroscopy of Gases and Liquids*; Weber, A., Ed.; Springer-Verlag: Berlin, Heidelberg, New York, 1979; pp 123–166.
- (31) Jordan, A.; Steinberg, B. Calibration of atmospheric hydrogen measurements. *Atmos. Meas. Tech.* **2011**, *4*, 509–521.
- (32) Magnotti, G.; KC, U.; Varghese, P.; Barlow, R. Raman spectra of methane, ethylene, ethane, dimethyl ether, formaldehyde and propane for combustion applications. *J. Quant. Spectrosc. Radiat. Transf.* **2015**, *163*, 80–101.
- (33) Lan, X.; Thoning, K.; Dlugokencky, E. Trends in globally-averaged CH4, N2O, and SF6 determined from NOAA Global Monitoring Laboratory measurements. Version 2022-10. https://gml.noaa.gov/ccgg/trends\_ch4/.
- (34) Van Helvoort, K.; Knippers, W.; Fantoni, R.; Stolte, S. The Raman spectrum of ethane from 600 to 6500 cm- 1 stokes shifts. *Chem. Phys.* **1987**, *111*, 445–465.
- (35) Marzouk, H. A.; Bradley, E. B. Normal unenhanced Raman spectra of 13CO adsorbed on Ni (111): A comparison study. *Spectrosc. Lett.* **1985**, *18*, 791–814.
- (36) Knebl, A.; Domes, R.; Yan, D.; Popp, J.; Trumbore, S.; Frosch, T. Fiber-enhanced Raman gas spectroscopy for 18O–13C-labeling experiments. *Anal. Chem.* **2019**, *91*, 7562–7569.

- (37) Franco, B.; Mahieu, E.; Emmons, L.; Tzompa-Sosa, Z.; Fischer, E.; Sudo, K.; Bovy, B.; Conway, S.; Griffin, D.; Hannigan, J., et al. Evaluating ethane and methane emissions associated with the development of oil and natural gas extraction in North America. *Environ. Res. Lett.* **2016**, *11*, 044010.
- (38) Defratyka, S. M.; Paris, J.-D.; Yver-Kwok, C.; Loeb, D.; France, J.; Helmore, J.; Yarrow, N.; Gros, V.; Bousquet, P. Ethane measurement by Picarro CRDS G2201-i in laboratory and field conditions: potential and limitations. *Atmos. Meas. Tech.* **2021**, *14*, 5049–5069.
- (39) Chen, X.; Wreyford, R.; Nasiri, N. Recent Advances in Ethylene Gas Detection. *Materials* **2022**, *15*, 5813.
- (40) Chang, C. Q&A: How do plants respond to ethylene and what is its importance? *BMC Biol.* **2016**, *14*, 1–7.
- (41) Jochum, T.; Rahal, L.; Suckert, R. J.; Popp, J.; Frosch, T. All-in-one: A versatile gas sensor based on fiber enhanced Raman spectroscopy for monitoring postharvest fruit conservation and ripening. *Analyst* **2016**, *141*, 2023–2029.
- (42) Metsälä, M.; Schmidt, F. M.; Skyttä, M.; Vaittinen, O.; Halonen, L. Acetylene in breath: background levels and real-time elimination kinetics after smoking. *J. Breath Res.* **2010**, *4*, 046003.
- (43) Marchenko, D.; Neerincx, A.; Mandon, J.; Zhang, J.; Boerkamp, M.; Mink, J.; Cristescu, S.; Hekkert, S. t.; Harren, F. A compact laser-based spectrometer for detection of C2H2 in exhaled breath and HCN in vitro. *Appl. Phys. B* **2015**, *118*, 275–280.
- (44) Gantt, B.; Owen, R. C.; Watkins, N. Characterizing nitrogen oxides and fine particulate matter near major highways in the United States using the national near-road monitoring network. *Environ. Sci. Technol.* **2021**, *55*, 2831–2838.
- (45) Lundberg, J.; Weitzberg, E. Nasal nitric oxide in man. Thorax 1999, 54, 947–952.

- (46) Avetisov, V.; Bjoroey, O.; Wang, J.; Geiser, P.; Paulsen, K. G. Hydrogen sensor based on tunable diode laser absorption spectroscopy. *Sensors* **2019**, *19*, 5313.
- (47) Schultealbert, C.; Amann, J.; Baur, T.; Schütze, A. Measuring Hydrogen in Indoor Air with a Selective Metal Oxide Semiconductor Sensor. *Atmosphere* **2021**, *12*, 366.
- (48) Chauhan, P. S.; Bhattacharya, S. Hydrogen gas sensing methods, materials, and approach to achieve parts per billion level detection: A review. *Int. J. Hydrog. Energy* **2019**, *44*, 26076–26099.
- (49) Darmadi, I.; Nugroho, F. A. A.; Langhammer, C. High-performance nanostructured palladium-based hydrogen sensors—current limitations and strategies for their mitigation. *ACS Sens.* **2020**, *5*, 3306–3327.
- (50) Kim, K.-H.; Jahan, S. A.; Kabir, E. A review of breath analysis for diagnosis of human health. *Trends in Anal. Chem.* **2012**, 33, 1–8.